Atomistic simulations of kinks in $1/2a\langle 111\rangle$ screw dislocations in bcc tantalum

Guofeng Wang,* Alejandro Strachan,† Tahir Çağın, and William A. Goddard III‡
Materials and Process Simulation Center, Beckman Institute (139-74), California Institute of Technology, Pasadena, California 91125, USA

(Received 16 May 2003; revised manuscript received 12 August 2003; published 5 December 2003)

Two types of equilibrium core structures (denoted symmetric and asymmetric) for $1/2a\langle 111\rangle$ screw dislocations in bcc metals have been found in atomistic simulations. In asymmetric (or polarized) cores, the central three atoms simultaneously translate along the Burgers vector direction. This collective displacement of core atoms is called polarization. In contrast, symmetric (nonpolarized) cores have zero core polarization. To examine the possible role of dislocation core in kink-pair formation process, we studied the multiplicity, structural features, and formation energies of $1/3a\langle 112\rangle$ kinks in $1/2a\langle 111\rangle$ screw dislocations with different core structures. To do this we used a family of embedded atom model potentials for tantalum (Ta) all of which reproduce bulk properties (density, cohesive energy, and elastic constants) from quantum mechanics calculations but differ in the resulting polarization of $1/2a\langle 111\rangle$ screw dislocations. For dislocations with asymmetric core, there are two energy equivalent core configurations [with positive (P) and negative (N) polarization], leading to 2 types of (polarization) flips, 8 kinds of isolated kinks, and 16 combinations of kink pairs. We find there are only two elementary kinks, while the others are composites of elementary kinks and flips. In contrast, for screw dislocations with symmetric core, there are only two types of isolated kinks and one kind of kink pair. We find that the equilibrium dislocation core structure of $1/2a\langle 111\rangle$ screw dislocations is an important factor in determining the kink-pair formation energy.

DOI: 10.1103/PhysRevB.68.224101 PACS number(s): 62.20.Fe, 61.72.Lk

I. INTRODUCTION

Plastic deformation in metals and semiconductors is controlled by the properties of dislocations and the interactions of dislocations with each other and with other defects in the crystal. Hence, knowledge of the structure, self-energy, and evolution patterns of dislocations is essential for understanding plastic deformation of materials and for developing mesoscopic models of deformation processes.[1–4] Useful information on dislocations has been obtained from such high-resolution experimental techniques as high-resolution transmission electron microscopy (HRTEM) and scanning tunneling microscopy (STM), however, many important details of the structural and energetic properties of dislocations remain beyond the resolution of current experimental methods. Thus atomistic computer simulations are needed to provide insight about the nature and properties of dislocations.[5,6]

In bcc metals at low temperatures, the crystal lattice resists to the motion of screw dislocations more strongly than to edge dislocations.[7] Thus, the mobility of screw dislocations governs the plastic deformation behavior of these materials in this temperature range. In previous atomistic simulations at zero temperature,[8–11] the screw dislocation has been considered to move in a rigid, collective fashion leading to Peierls stresses of about $10^{-2}\ \mu$ (where μ is the shear modulus of the crystal). However, the observation of a rapid decrease of the Peierls stress with increasing temperature implies that at finite temperatures the screw dislocations move by formation and subsequent migration of kinks pairs rather than by translation of a straight dislocation.[12] The kink is a piece of dislocation connecting a dislocation segment that is in an equilibrium position to another segment in a neighboring equilibrium position.

The concept of kinks and the role of kinks in describing plastic flow behavior of crystal were first treated mathematically in the framework of elasticity theory by Seeger and Schiller.[13] Kolar *et al.*[14] made the first direct observation of the dislocation kinks using atomic resolution transmission electron microscopy (TEM) on partial dislocations in Si. In the last two decades, many mesoscale plasticity models (for instance, Ref. 4) use the kink-pair mechanism to describe the motion of dislocations. These theoretical models require an accurate description of dislocation kinks, which can be provided by atomistic simulations.

Based on atomistic simulations, Seeger *et al.*[15] proposed that the dislocation cores for $1/2a\langle 111\rangle$ screw dislocations in α-Fe were polarized and then explained the multiplicity of kinks and the existence of (polarization) flips. In two classical papers,[16,17] Duesbery studied the structures, Peierls stresses, and formation energies of the isolated kinks in $1/2a\langle 111\rangle$ screw dislocations in K and α-Fe. Later, Duesbery and Basinski[18] showed that the atomistic simulation results for kink pair generation and migration agreed with the experimental flow stress data for potassium (K). Recently, the formation energies of kinks in screw dislocations in Ta (Ref. 9) and Mo (Ref. 19) have been determined much more accurately in simulations using Green's function boundary conditions.

In bcc metals, two types of screw dislocation cores have been found in atomistic simulations (asymmetric cores in Refs. 20, 21, and 22 and symmetric cores in Refs. 9, 22, 23, and 24). In this paper, we investigate how the character of the equilibrium core structure (asymmetric or symmetric) affects the properties of the kinks in $1/2a\langle 111\rangle$ screw dislocations using Ta as a model bcc metal. To do that, we developed a family of first-principles-based force fields (FFs) for Ta. Each force field is optimized to fit a range of properties from the *ab initio* calculations, but adjusted to have very

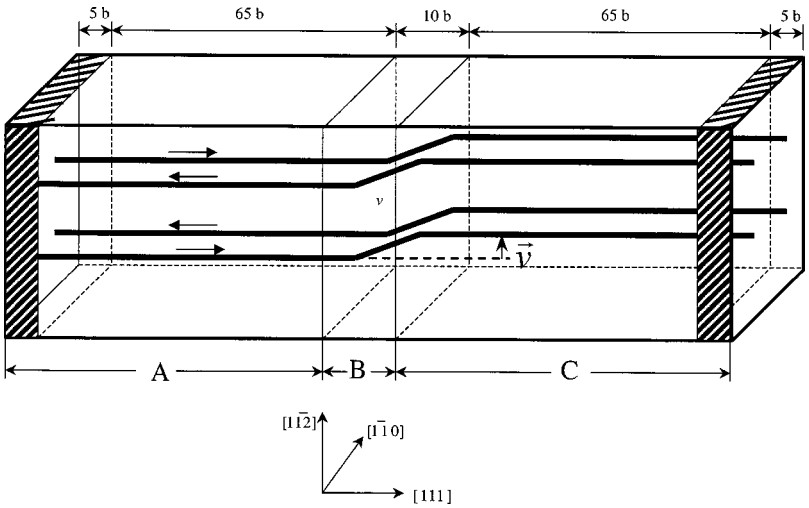

FIG. 1. The schematic representation of the model system used in simulations. In this model, regions *A* and *C* contain the equilibrium dislocation quadruples. Atomic positions in region *B* are determined based on elasticity theory to smooth out the configuration misfit. The vector $\boldsymbol{\nu}$ starts from the center of the dislocation in region *A* and points to the dislocation in the region *C*. In our simulations, $\boldsymbol{\nu}$ can only be 0 (flips), $1/3a[11\bar{2}]$ (right kinks) or $1/3a[\bar{1}12]$ (left kinks). The shaded regions indicate the fixed boundaries, which are $5b$ thick, in the simulation. The cell parameters are $5a[11\bar{2}]$, $9a[1\bar{1}0]$, and $150a/2[111]$.

different dislocation core characters. This leads to three force fields, which we denote as *q*EAM*i* ($i=1$, 2, and 3). We have recently used this family of force fields to study the relation between Peierls stresses and core properties of $1/2a\langle 111\rangle$ screw dislocations in bcc Ta.[25] In this paper, we show how the multiplicity, structural features, and formation energies of $1/3a\langle 112\rangle$ kinks for $1/2a\langle 111\rangle$ screw dislocations depend on the character (asymmetric or symmetric) of dislocation cores.

The remainder of the paper is organized as follows. Section II describes the details of the periodic/fixed boundary simulation models used in the calculations. Section III describes the different core configurations of $1/2a\langle 111\rangle$ screw dislocations and the differences in our *q*EAM FFs. Section IV reports our results on the multiplicity, structural features, and formation energies of the isolated kinks in $1/2a\langle 111\rangle$ screw dislocations with asymmetric cores. Section IV also summarizes and explains the trend of the kink formation energy for screw dislocations with asymmetric core. Further we discuss the inherent relationship between different kinks. Section V reports our results of kink properties for $1/2a\langle 111\rangle$ screw dislocations with symmetric core. Finally, our conclusions and further discussion are given in Sec. VI.

II. THE PERIODIC/FIXED BOUNDARY SIMULATION MODEL

A. Description of simulation model

To study kinks in dislocations, we use the simulation model shown schematically in Fig. 1. The model is orthorhombic and the three axes are aligned with the $[11\bar{2}]$, $[1\bar{1}0]$, and [111] crystal directions. To construct kinks we consider three distinct regions (denoted as *A*, *B*, and *C* in Fig. 1) in the [111] direction.

Regions *A* and *C* contain four equilibrium $a/2\langle 111\rangle$ screw dislocations arranged as a quadrupole, in which there are one pair of dislocations with Burgers vector $b=a/2[111]$ and one pair of dislocations with Burgers vector $b=a/2[\bar{1}\bar{1}1]$. The atomic positions in regions *A* and *C* were obtained by energy minimization using the *q*EAM FFs for a three-dimensional periodic cell containing perfect straight dislocations initially constructed with elasticity theory. The positions of the dislocations in regions *A* and *C* differ by a vector $\boldsymbol{\nu}$ (pointing from the equilibrium dislocation center in region *A* to the equilibrium dislocation center in region *C* as indicated in Fig. 1).

The initial atomic displacements relative to the perfect crystal for atoms in region *B* (representing the unrelaxed kink) were obtained from elasticity theory by the following equations:

$$\Delta d^{B}_{[111]}(\mathbf{r}) = (1-\alpha)\cdot \Delta d^{A}_{[111]}(\mathbf{r}) + \alpha \cdot \Delta d^{C}_{[111]}(\mathbf{r}) \qquad (1)$$

with

$$\alpha = \frac{h(\mathbf{r})}{h_B}, \qquad (2)$$

where $\Delta d^{A}_{[111]}(\mathbf{r})$ and $\Delta d^{C}_{[111]}(\mathbf{r})$ are the atomic displacements determined from elasticity theory for the atom positioned at $\mathbf{r}$ in the region *B* caused by the periodic dislocation quadruples in regions *A* and *C*, respectively. The origin of $\mathbf{r}$ is set as the left-front corner of the region *B*. h_B is the height of the region *B* in the [111] direction, and $h(\mathbf{r})$ is the distance in the [111] direction from this atom to the interface between the regions *A* and *B*. Thus, $\Delta d^{B}_{[111]}(\mathbf{r}) = \Delta d^{A}_{[111]}(\mathbf{r})$ at the boundary between regions *A* and *B*, $\Delta d^{B}_{[111]}(\mathbf{r}) = \Delta d^{C}_{[111]}(\mathbf{r})$ at the boundary between regions *B* and *C*, $\Delta d^{B}_{[111]}(\mathbf{r})$ is a linear combination of $\Delta d^{A}_{[111]}(\mathbf{r})$ and $\Delta d^{C}_{[111]}(\mathbf{r})$ depending on $h(\mathbf{r})/h_B$ inside the region *B*. Therefore, the central region *B* is constructed to smooth out the interfacial misfit between regions *A* and *C*.

After constructing the initial kink as described above, we relaxed the whole model crystal to its minimum energy state. The obtained kinks in the screw dislocations are found to be smooth and continuous. In these simulations, we imposed periodic boundary conditions on both $(11\bar{2})$ and $(1\bar{1}0)$ surfaces and fixed boundary conditions on both ends of the simulation cell in the [111] direction. The fixed regions are $5b$ ($\sim$14.4 Å) thick [larger than the cutoff radius (9 Å) of the *q*EAM FFs] and the atomic positions there correspond to the equilibrium dislocation quadruples. Thus, the movable atoms

interacting with the fixed boundaries in the simulation effectively interact with an infinite equilibrium dislocation quadruple.

Our studies employed a simulation cell whose geometry was $5a[11\bar{2}]$, $9a[\bar{1}10]$, and $150a/2[111]$. As indicated in Fig. 1, the length of regions *A*, *B*, and *C* are $L_A=70b$, $L_B=10b$, and $L_C=70b$, respectively. Our model contains 40 500 atoms (37 800 movable) in the simulation cell.

B. Evaluation of the kink formation energy

The atomic strain energy is defined to be the energy for each atom in the model system minus the atomic cohesive energy in perfect bcc crystal. We calculated the total strain energy of the relaxed simulation cell $[E_d(\text{cell})]$ by summing the atomic strain energies for all movable atoms in the simulation cell. This energy includes the self-energies of the defective (kink or flip) dislocations $[E_d(\text{self})]$ and the interaction energy between them $[E_d(\text{inter})]$. In the case of a quadrupole of perfect (straight) dislocations in equilibrium, the total energy $[E_p(\text{cell})]$ can also be calculated with simple 3D periodic boundary conditions (the fixed boundaries in Fig. 1 are removed). This total energy $E_p(\text{cell})$ can also be expressed as the self-energy of the perfect dislocation $[E_p(\text{self})]$ plus the interaction energy between the perfect dislocations $[E_p(\text{inter})]$.

The dislocation defect (kink or flip) formation energy is the self-energy difference between the isolated dislocation with the defect and the perfect dislocation. Thus the intrinsic defect formation energy (ΔE_f) is expressed as

$$\Delta E_f=\frac{1}{4}[E_d(\text{cell})-E_p(\text{cell})]-\frac{1}{4}[E_d(\text{inter})-E_p(\text{inter})]. \tag{3}$$

In Eq. (3), the first term $\frac{1}{4}[E_d(\text{cell})-E_p(\text{cell})]$ (the differential cell energy) is obtained directly from the simulations while the second term $-\frac{1}{4}[E_d(\text{inter})-E_p(\text{inter})]$ (the interaction correction) is nonzero only for kinks (a flip does not affect the elastic behavior of a dislocation) and in this work is obtained from elasticity theory.

The interaction energy between two dislocations with kinks and the interaction energy between two straight dislocations can be calculated by summing the interaction contributions from all piecewise straight segments. This approach has been used to derive the elastic energy of the kink pair in the same dislocation.[26] Thus, the converged value of the second term in Eq. (3) can be obtained by summing the pair interactions in the 2D periodic quadruple of the kinked dislocations and the straight dislocations.

Approximating the shape of the kink as straight dislocation segment with width *w* along the dislocation line and height *h* normal to the dislocation and using isotropic elasticity, we calculated the interaction energy difference between a pair of dislocations with kink and a pair of straight dislocations, denoted as $W(L_1,L_2)$, using the following equations:

$$R_0(L_1,L_2)=2\sqrt{L_1^2+L_2^2}-\sqrt{L_1^2+(L_2-h)^2}-\sqrt{L_1^2+(L_2+h)^2}, \tag{4a}$$

$$R_w(L_1,L_2)=2\sqrt{L_1^2+L_2^2}-\sqrt{w^2+L_1^2+(L_2-h)^2}-\sqrt{w^2+L_1^2+(L_2+h)^2}, \tag{4b}$$

$$I(L_1,L_2)=R_w(L_1,L_2)-\frac{2hL_2}{\sqrt{w^2+h^2}}\ln\left[\sqrt{L_1^2+L_2^2}+\frac{hL_2}{\sqrt{w^2+h^2}}\right]+\frac{hL_2+w^2+h^2}{\sqrt{w^2+h^2}}\ln\left[\sqrt{w^2+L_1^2+(L_2+h)^2}+\frac{hL_2+w^2+h^2}{\sqrt{w^2+h^2}}\right]$$
$$+\frac{hL_2-w^2-h^2}{\sqrt{w^2+h^2}}\ln\left[\sqrt{w^2+L_1^2+(L_2-h)^2}+\frac{hL_2-w^2-h^2}{\sqrt{w^2+h^2}}\right], \tag{4c}$$

$$W(L_1,L_2)=\frac{\mu b_1 b_2}{4\pi}\left[R_0(L_1,L_2)+\frac{w^2}{w^2+h^2}I(L_1,L_2)\right]+\frac{\mu b_1 b_2}{4\pi(1-\nu)}\left[\frac{h^2L_1^2\cdot[I(L_1,L_2)+R_w(L_1,L_2)]}{h^2L_1^2+w^2(L_1^2+L_2^2)}+\frac{h^2w^2L_2^2\cdot I(L_1,L_2)}{(w^2+h^2)[h^2L_1^2+w^2(L_1^2+L_2^2)]}\right]. \tag{4d}$$

In the above equations, L_1 and L_2 are the separation distances between dislocations in the $[11\bar{2}]$ and $[\bar{1}10]$ directions; *w* and *h* are the kink width and kink height, respectively; b_1 and b_2 are the Burgers vectors of the two dislocations. The shear modulus μ is equal to C_{44} and the Poisson ratio $\nu=C_{12}/(C_{11}+C_{12})$.

III. EQUILIBRIUM DISLOCATION CORE STRUCTURES

A. Asymmetric core and symmetric core

We used elasticity theory to construct the initial simulation cell with a screw dislocation quadruple. Then, we used the various *q*EAM FFs (see Sec. III B) to minimize the total

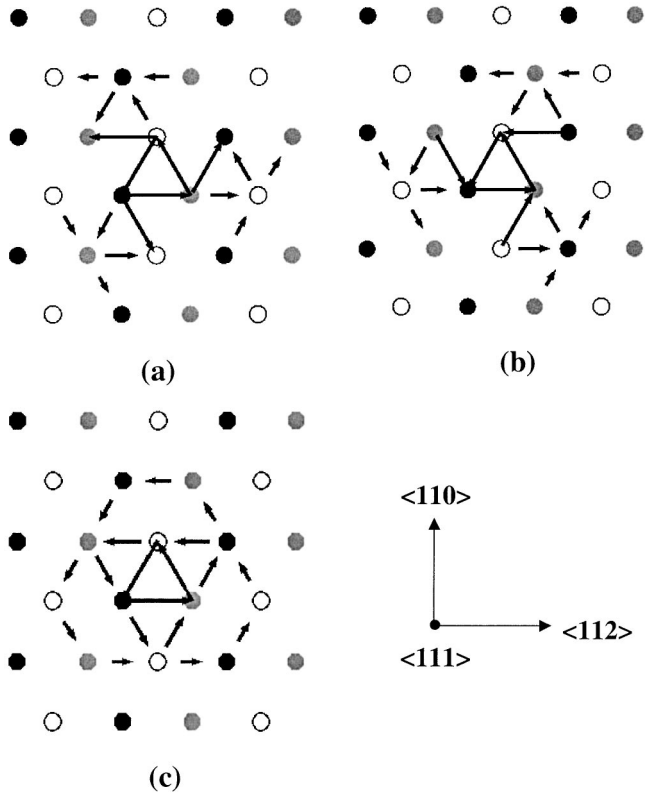

FIG. 2. The differential displacement maps for the equilibrium dislocation core configurations: (a) *N*-type asymmetric core, (b) *P*-type asymmetric core, and (c) symmetric core. The [111] direction is normal to the paper. For clarity, the relative displacements less than 1/12 *b* are not shown in the figures.

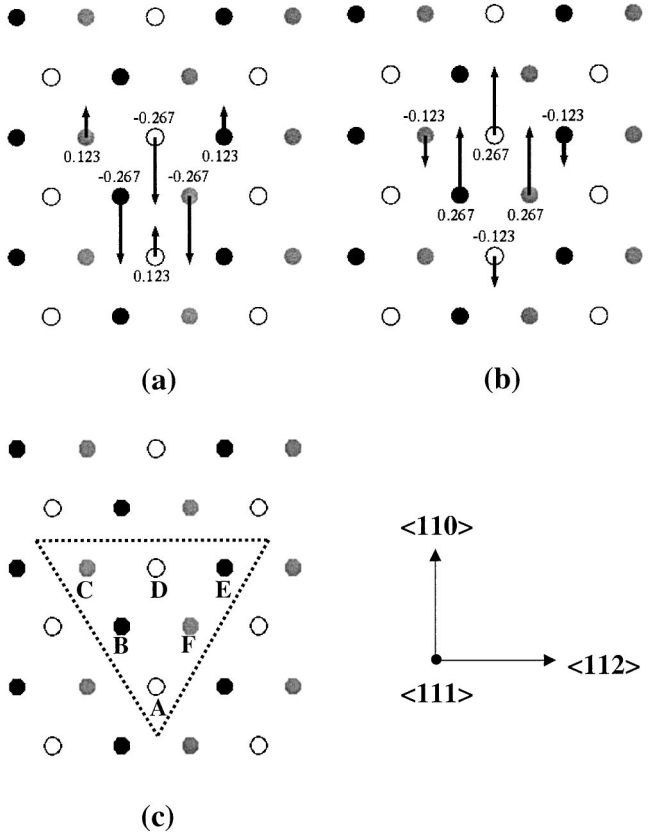

FIG. 3. The relaxation maps for the equilibrium dislocation core configurations: (a) *N*-type asymmetric core, (b) *P*-type asymmetric core, and (c) symmetric core. The [111] direction is normal to the paper. The magnitudes of such relaxation (in Å) for the central six columns of atoms (the relaxation for the other atoms is less than 0.05 Å) are printed next to the corresponding atom.

energy of the quadruple to obtain the equilibrium dislocation configuration. We find for $1/2a\langle 111\rangle$ screw dislocations that *q*EAM1 FF leads to an asymmetric screw dislocation core while both the *q*EAM2 and *q*EAM3 FFs lead to symmetric dislocation core configurations. In the following we show the difference between two types of core structures by using differential displacement maps, relaxation maps, planar displacement maps, and atomic strain energy distributions.

1. Differential displacement maps

The differential displacement (DD) maps[20] in Fig. 2 show the strain field generated by the screw dislocations. In these plots, the circles represent atomic positions projected in the (111) plane and the arrows indicate the relative displacements in the [111] direction of the neighboring atoms with reference to their positions in the perfect bcc crystal. Among the projected atoms, black circles stand for the atoms farthest from the reader while shaded circles represent the atoms closest to the reader in the [111] direction, which is perpendicular to the map. The *direction* of the arrow represents the sign of the relative displacement and the *magnitude* is proportional to the relative displacement between the corresponding atoms. When the arrow touches the centers of the two atoms, the relative displacement between these two atoms is $b/3$.

Figures 2(a) and 2(b) show the DD maps for two equilibrium asymmetric dislocation cores from the *q*EAM1 FF simulations. These figures show that the asymmetric core spreads out in three $\langle 112\rangle$ directions on the $\{110\}$ planes. There are six equivalent $\langle 112\rangle$ directions on the projected (111) plane, leading to two kinds of asymmetric core configurations that are energy degenerate. In contrast, Fig. 2(c) shows that the equilibrium dislocation core predicted from both *q*EAM2 and *q*EAM3 FFs are symmetric and compact with no preferential extension in any direction. Thus, this type of the dislocation core is called symmetric core.

In bcc crystals, the asymmetric core breaks the twofold rotation symmetries (C_2) around the three $\langle 110\rangle$ directions perpendicular to the dislocation axis while the symmetric core has full D_3 symmetry.[23]

2. Relaxation maps

Figures 3(a) and 3(b) depict the differences in the [111] displacement for each atom between the relaxed positions obtained with *q*EAM1 FF and those calculated using elasticity theory. In these plots, the circles represent the same projected atoms in the (111) plane as those in Figs. 2(a) and 2(b) and only the direction and magnitude of the [111] displacement differences for the central six columns of atoms are displayed. The magnitude of the [111] displacement differences for all other atoms except the six columns closest to

the dislocation line is less than 0.05 Å ($0.017b$). The most important result in these maps is that the three central atoms of the dislocation relax simultaneously by 0.267 Å ($0.09b$) in the [111] direction for an *N*- (negative) type core [shown in Figs. 2(a) and 3(a)] or in the [111] direction for the *P*- (positive) case [shown in Figs. 2(b) and 3(b)]. This phenomenon is called dislocation polarization.[15] We find that the *P*-type dislocation cores spread along the [1 1 2], [1 2 1], and [2 1 1] directions while the *N*-type dislocation cores spread along the [1 1 2], [1 2 1], and [2 1 1] directions in the DD maps, regardless of the orientation of Burgers vector.

We define the magnitude of the dislocation core polarization by Eq. (5):

$$p = \frac{|d_{BC} - d_{AB}| + |d_{DE} - d_{CD}| + |d_{FA} - d_{EF}|}{b}, \qquad (5)$$

where d_{XY} (X, $Y = A$, B, C, D, E, or F) is the relative displacement between two neighboring atoms in the two columns denoted as X and Y in Fig. 3(c) and b is the magnitude of the dislocation Burgers vector. Using Eq. (5), the polarization for the asymmetric core from the qEAM1 FF is $p = 0.81$. Our definition [Eq. (5)] of dislocation polarization is equivalent to the previous definition proposed in Ref. 9. We favor the definition presented here because it is solely based on the relaxed atomic positions of the central six atoms in the dislocation core. In contrast, the previous definition only considers the relaxation of the central three atoms and requires a comparison with the elasticity theory solution.

On the other hand, the relaxation map for the symmetric cores does not show any major relaxation in the [111] direction between the atomistic results and the elasticity theory predictions [see Fig. 3(c)]. Using the definition in Eq. (5) the symmetric cores obtained from the qEAM2 or qEAM3 FFs have polarization of only about 10^{-4}. Thus, polarization is a useful quantity to distinguish the asymmetric and symmetric dislocation cores.

3. Planar displacement maps

Planar displacement maps display the atomic displacements in the (111) plane for the atoms close to the dislocation line. Figure 4 shows the planar displacement maps for $1/2a\langle 111\rangle$ screw dislocations with an *N*-type asymmetric core [Fig. 4(a)], a *P*-type asymmetric core [Fig. 4(b)], and a symmetric core [Fig. 4(c)]. In these maps, the circles represent the same atoms as those in the DD maps (Fig. 2) and relaxation maps (Fig. 3). The arrows here indicate the atomic displacement for each atom in the (111) plane between the relaxed screw dislocation and the perfect bcc lattice.

In the asymmetric dislocation cores from our qEAM1 FF simulations, the central three atoms (atom *B*, *D*, and *F* in the figure) are displaced in the (111) plane by 0.08 Å, the atoms *A*, *C*, and *E* by 0.09 Å, and all the other atoms by less than 0.06 Å.

In contrast, the planar atomic displacements for the symmetric core are much smaller (0.003 Å for the atoms *B*, *D*, and *F*, 0.011 Å for the atoms *A*, *C*, and *E*, and less than 0.009 Å for the other atoms).

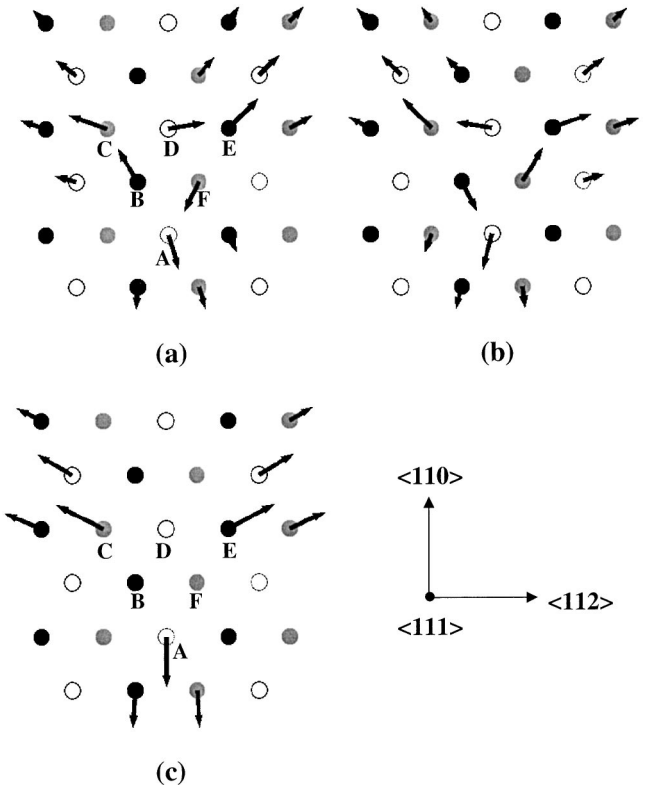

FIG. 4. The planar displacement maps for the equilibrium dislocation core configurations: (a) *N*-type asymmetric core, (b) *P*-type asymmetric core, and (c) symmetric core. The [111] direction is normal to the paper. To show clearly the spatial distribution of the in-plane displacements, the arrows have been magnified by a factor of 20 in asymmetric cores [(a) and (b)] and a factor of 200 in symmetric core [(c)] with reference to the lattice constant. For clarity, the atomic displacements less than 0.04 Å are not shown in (a) and the displacements less than 0.004 Å are not shown in (b).

In addition to the magnitudes, the in-plane atomic displacements for asymmetric cores and symmetric cores have different spatial distributions. All the in-plane atomic displacements around a symmetric core are in the radial direction starting from the dislocation center. However, the displacements around the asymmetric cores deviate from the radial direction originating from the dislocation center. For instance, the (111) atomic displacements for atoms *B*, *D*, and *F* rotate by about 81° (clockwise for the *N*-type asymmetric core and anticlockwise for the *P*-type asymmetric core) from the radial direction; while the displacements for the atoms *A*, *C*, and *E* rotate by a smaller angle of about 15° (anticlockwise for the *N*-type asymmetric core and clockwise for the *P*-type asymmetric core).

There is not yet any convincing experimental evidence showing whether the core of $1/2a\langle 111\rangle$ screw dislocations is asymmetric or symmetric in bcc metals. These planar displacement maps should be helpful for interpreting the high-resolution transmission electron microscopic (HRTEM) characterizations of screw dislocation core structures in bcc metals. For example, to reach a concrete conclusion, the previous experimental results in Ref. 27 should be analyzed by focusing only on the central six atoms.

TABLE I. Experimental and theoretical values of lattice parameter a (Å), elastic moduli C_{11} (GPa), C_{12} (GPa), and C_{44} (GPa), and the shear modulus in the ⟨111⟩ direction G (GPa) $[G=(C_{11}-C_{12}+C_{44})/3]$ for bcc Ta from our qEAM force fields, the MGPT FF, and experiments.

	a	C_{11}	C_{12}	C_{44}	G
qEAM1	3.32	273	138	69.6	68.2
qEAM2	3.35	255	148	60.2	55.7
qEAM3	3.32	257	148	77.3	62.1
MGPT[a]	3.30	266	161	82.5	62.5
Expt.[b]	3.30	266	158	87.4	65.1

[a]Reference 9.
[b]Reference 40.

4. Atomic strain energy distribution

As already mentioned the strain energy associated with each atom in the simulations is calculated as the difference between the atomic energy in the model crystal compared to the atomic energy in the perfect bcc crystal. We calculated the atomic strain energy distributions for the relaxed dislocation quadruple with 5670 atoms (with cell size $\mathbf{X}=9\langle 112\rangle a$, $\mathbf{Y}=15\langle 110\rangle a$, and $\mathbf{Z}=7/2\langle 111\rangle a$). In the asymmetric dislocation core (obtained using the qEAM1 FF), a group of six atoms has atomic strain energies between 0.155 to 0.175 eV, a second group of six atoms has atomic strain energies ranging from 0.065 to 0.085 eV, and the other atoms have atomic strain energies less than 0.05 eV. In comparison, in the symmetric dislocation core (obtained using the qEAM2 FF), there is only one group of six atoms with atomic strain energies higher than 0.05 eV. Their atomic strain energies range from 0.175 to 0.195 eV, which is larger than the energy range of the first group of six atoms in an asymmetric core. In both types of dislocation cores, the six atoms with the highest atomic strain energies are closest to the dislocation line corresponding to the six atoms lettered in Fig. 3(c).

B. Differences in our three qEAM FFs

In our study, the interactions among atoms are described using a family of embedded atom model potentials (denoted qEAM FFs) developed to reproduce a large quantity of data obtained from quantum mechanics calculations. The functional form is based on that proposed by Chantasiriwan and Milstein.[28] All the qEAM FFs were parametrized to the same set of *ab initio* data that includes: (i) zero temperature energy and pressure as a function of volume (including large compressions and expansions) for various phases bcc, fcc, and $A15$, (ii) elastic constants, (iii) vacancy and surface formation energies, and (iv) energetics of a shear deformation in the twinning direction that takes the bcc crystal back to itself. Reference 29 gives the details of the force field optimization procedure.

Table I shows that the three qEAM FFs lead to similar lattice parameters and elastic constants for bcc Ta at 0 K. Moreover, they also lead to similar generalized staking fault (also known as γ surface) energies in Fig. 5(a) for the ⟨111⟩ direction in the {112} plane and Fig. 5(b) for the ⟨111⟩ direction in the {110} plane. The results for qEAM1 FF agree very well with the accurate *ab initio* data.[9] The γ surface, which is the energy profile of two semi-infinite half crystals first displaced relative to each other by a vector on a crystallographic plane and then relaxed only in the direction perpendicular to the plane, is considered as an important validation for the accurate modeling bcc screw dislocation behavior.[20] Since the γ surfaces ⟨111⟩/{112} and ⟨111⟩/{110} are low energy processes, the quantitative agreement in these two cases is expected to be most important.[9]

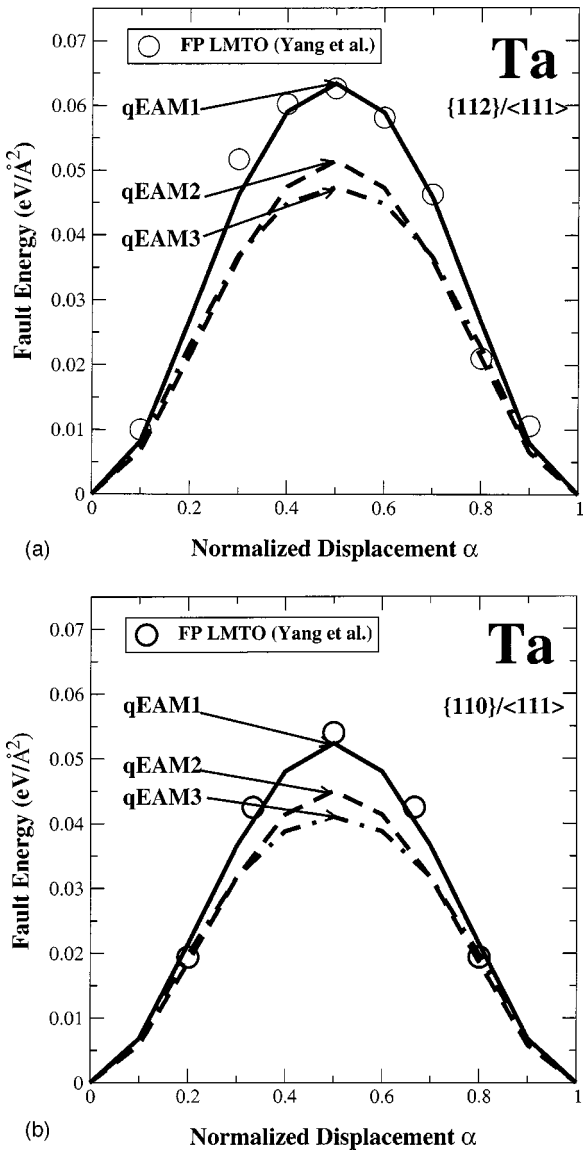

FIG. 5. (a) The ⟨111⟩ line in the {112} plane and (b) the ⟨111⟩ line in the {110} plane γ surface energies for bcc Ta as calculated with the qEAM potentials and the *ab initio* method. In the qEAM calculations, fixed boundary conditions are applied after either 48 {112} atomic planes or 16 {110} atomic planes on both sides of the faulted surface.

As described above the qEAM FFs were devised to produce bulk properties results in good agreement with QM calculations. Furthermore, we deliberately constraint these

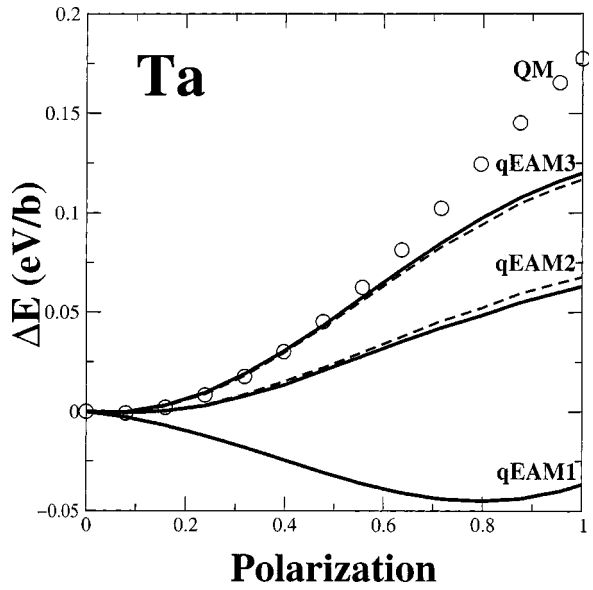

FIG. 6. The dependence of the dislocation core energy with its polarization from our qEAM FFs and from DFT-LDA calculations. The solid lines in the figure show the energy difference for the relaxed structures using the qEAM FFs, while the dashed lines show the results from the energy evaluation of the relaxed structures from the qEAM1 FF. The QM results are shown as circles.

force fields to provide different core polarization behaviors for screw dislocations. Figure 6 shows the relative energy (the energy difference between the polarized asymmetric cores and the zero polarization symmetric core) as a function of polarization for the various qEAM FFs. To obtain the energies for the nonequilibrium core configurations, we fixed the positions of the six atoms [atoms A to F in Fig. 3(c)] in the direction of the dislocation line and optimized the energy for all other atoms. All calculations used a periodic simulation cell with parameters of $\mathbf{X}=3a[11\bar{2}]$, $\mathbf{Y}=5a[1\bar{1}0]$, and $\mathbf{Z}=1/2a[111]$ (90 atoms per cell) and the quadruple dislocation arrangement.

The open circles in Fig. 6 show the energies (without structural relaxation) from density-functional theory (DFT) with the local density approximation (LDA)[30,31] using the relaxed atomic configurations obtained from the qEAM1 FF. These calculations used Hamann type generalized norm-conserving pseudopotential for Ta with nonlinear core correction.[32,33] We used eight k points in the direction of the dislocation line and one k point in the normal directions. These calculations predict the symmetric core with the lowest energy, which is consistent with the previous *ab initio* results from direct minimization.[23,24] Although we did not optimize the atomic configurations in the DFT-LDA calculations, the fact that the relative energies change very little when using the qEAM FFs (dashed lines represent the unrelaxed FF calculations in Fig. 6) indicates that fully optimization is unnecessary.

In summary, the three force fields lead to similar properties for Ta except with regard to dislocation core polarization behavior:

(1) qEAM1 leads to an equilibrium asymmetric core with the polarization of 0.81 and the core polarization curvature (second derivative of core energy with respect to polarization around the equilibrium core configuration) of 0.171 eV.

(2) qEAM2 is adjusted to predict a symmetric dislocation core but with the core polarization curvature of 0.127 eV, which is close to the qEAM1 FF.

(3) qEAM3 leads to a symmetric core with the core polarization curvature of 0.285 eV very similar to that from our *ab initio* calculation.

We have used these qEAM FFs to predict the core energy and Peierls stresses for 1/2$a\langle 111\rangle$ screw dislocations and the results are in Table II. The dislocation core energy was obtained using the relaxed dislocation quadruple arrays with system sizes ranging from 1890 to 5670 atoms and the Peierls stress was determined by applying pure shears in various orientations for periodic simulation cells containing a [110] screw dislocation dipole with 11 466 atoms. More details on the computation procedure are in Refs. 11, 25, and 34. All three qEAM FFs lead to a larger core energy than the *ab initio* calculation[23] ($E_c=0.86$ eV/b, using a core radius $r_c=2b$), but the symmetric cores from the qEAM2 and qEAM3 FFs have similar core energies (~ 1.154 eV/b), only slightly lower than 1.297 eV/b (the core energy for the asymmetric core with qEAM1 FF). Despite their similar dislocation core structures and energies, the qEAM2 and qEAM3 FFs lead to dramatically different Peierls stresses,

TABLE II. The calculated core energy (eV/b) and Peierls stresses (in unit of shear modulus G) for 1/2a $\langle 111\rangle$ screw dislocations in bcc Ta using our qEAM FFs, the MGPT FF and the *ab initio* methods. χ is the angle between the plane with the maximum shear stress and the neighboring (110) plane.

	Core energy (eV/b)		Peierls stress (G)		
Force fields	$r_c=1.75b$	$r_c=2b$	$\chi=-30°$	$\chi=0°$	$\chi=30°$
qEAM1	1.190	1.297	0.0085	0.0117	0.0170
qEAM2	1.054	1.147	0.0065	0.0068	0.0108
qEAM3	1.063	1.161	0.0132	0.0138	0.0512
MGPT[a]	0.60		0.0096	0.0102	0.0223
ab initio		0.86[b]	0.012[c]	0.027[c]	0.064[c]

[a]Reference 9.
[b]Reference 23.
[c]Reference 41.

especially in the antitwinning direction ($\chi = 30°$). On the other hand, qEAM1 FF leads to a Peierls stress similar to qEAM2 FF for all shearing orientations even though they predict dramatically different core configurations. Reference 25 shows that the dominant factor underlying the magnitude of the Peierls stress in bcc materials is the core polarization curvature (defined above) because both symmetric and asymmetric cores require changes in the core polarization as a dislocation migrates from one equilibrium site to the next. Thus, the structure of the equilibrium dislocation core configurations has little effect on the Peierls stresses. The relevant quantity is how hard it is to change the polarization. In the next sections, we will explore the relationship between the dislocation core properties and the kink properties using these three qEAM FFs. Note that the qEAM2 in this work is actually the qEAM3 in Ref. 25 and the qEAM3 in this work is the qEAM4 in Ref. 25.

IV. KINKS IN ASYMMETRIC CORE SCREW DISLOCATIONS

A. Multiplicity

The two degenerate structures of the asymmetric core for $1/2a\langle 111\rangle$ screw dislocations (*N* and *P*) lead to two possible configurations of polarization flips (from *P* to *N* and from *N* to *P*) along the straight screw dislocation line. The *P-N* and *N-P* are two distinct flip configurations as shown in Fig. 7(a) with different formation energies. Regarding kinks, we focused our interest on those for which the dislocation segments are separated by either $1/3a[11\bar{2}]$ [called the right (*R*) kinks] or $-1/3a[11\bar{2}]$ [called the left (*L*) kinks]. Figure 7(b) shows in each category (right or left) of the kinks there are four combinations of the dislocation core configurations. This leads to eight possible kinks: *NRP*, *NRN*, *PRP*, *PRN*, *NLP*, *NLN*, *PLP*, and *PLN*. Note that the *NRN* and *PRP* kinks are energy degenerate, so are *NLN* and *PLP*.

B. Kink and kink pair formation energy

Following the descriptions in Sec. II B, Table III gives the calculated differential cell energy [first term of the Eq. (3)] from the simulation and the interaction correction [the second term of the Eq. (3)] from Eqs. (4). To determine the kink height h and the kink width w, we calculated the atomic-strain-energy-weighted center of the twelve atoms with the highest strain energies for each Burgers vector thick slice along the dislocation line. Our results show that the dislocation is in its equilibrium position in regions far away from the kink formation region. The kink formation region is the region $70b \leqslant Z \leqslant 80b$ shown in Fig. 1. Thus, the average distance between two equilibrium positions on the two sides of kink is the kink height h, which is equal to 2.71 Å ($|1/3a\langle 112\rangle|$) in our qEAM1 FF simulations. The kink width w can be estimated in the following way: the part of the dislocation in the kink formation region was fitted to a straight line, then the kink width w is the distance in the [111] direction between two intersections of this line with two equilibrium dislocation lines separated by the kink height. We find the kink width w is about $10.4b$ for all kinds of right kinks and $9.1b$ for all kinds of left kinks.

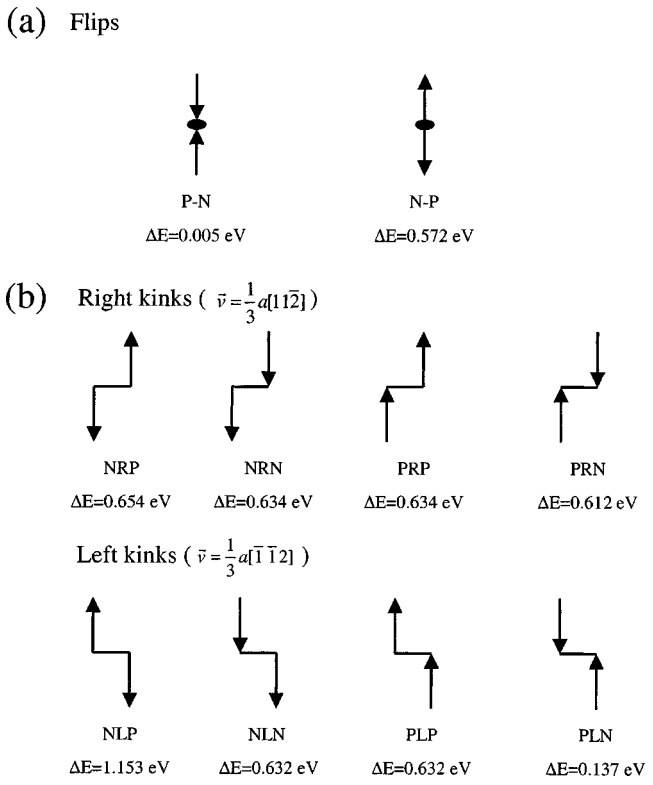

FIG. 7. The schematic drawing, nomenclature and calculated formation energies of the flips and kinks in the asymmetric core screw dislocations. In the figures, the triangle represents *P*-type dislocation and the upside down triangle represents *N*-type dislocation. (a) Two kinds of flips exist in screw dislocation. The core configuration along a straight dislocation line can flip either from *P* to *N* (denoted as *P-N*) or from *N* to *P* (denoted as *N-P*). (b) There are four kinds of right kinks (*NRP*, *NRN*, *PRP*, and *PRN*) and four kinds of left kinks (*NLP*, *NLN*, *PLP*, and *PLN*). The vector ν (indicated in Fig. 1) is $1/3a[11\bar{2}]$ for right kinks and $1/3a[\bar{1}\bar{1}2]$ for left kinks.

We chose the twelve atoms closest to the dislocation line with the highest atomic strain energies to represent the asymmetric dislocation core. This provides a definition of the dislocation core consistent with the atomic strain energy distribution for the equilibrium dislocation in Sec. III C. We also found in Ref. 34 that the twelve atoms with higher atomic strain energy describe well the variation in the asymmetric dislocation core during its translation. Although our results for the kink geometrical parameters might depend on the definition of dislocation core, the calculated kink formation energies are insensitive to it. Indeed, we find that the values of the interaction correction from the ''inclined'' model [Eq. (4)] deviate by only 0.001 eV for left kinks from the 0.030 eV obtained assuming the ''perpendicular'' kink model, in which the kink is a pure edge segment that is 2.71 Å ($|1/3a\langle 112\rangle|$) long in the $\langle 112\rangle$ direction. This indicates that even ignoring the real geometry of the kink causes only a marginal error in determining the kink formation energy (e.g., 0.7% for the *PLN* kink). We find that the *NRP* kink formation energy changes by 0.0003 eV and the *PLN* kink

TABLE III. The differential cell energies (eV) from the *q*EAM1 FF simulations, interaction corrections (eV) from continuum theory using the inclined model [Eq. (4)], and the intrinsic formation energies (eV) of the defects (flips and single isolated kinks) in $1/2a\ \langle 111\rangle$ screw dislocations in Ta. The *PRP* kink (not shown) has the same formation energy with the *NRN* kink, so does the *PLP* kink (not shown) with the *NLN* kink.

Configuration	Differential cell energy $\frac{1}{4}[E_d(\text{cell})-E_p(\text{cell})]$	Interaction correction[a] $-\frac{1}{4}[E_d(\text{inter})-E_p(\text{inter})]$	Intrinsic formation energy[b] ΔE_f
N-P(flip)	0.572	0	0.572
P-N(flip)	0.005	0	0.005
NRP(right kink)	0.624	0.030	0.654
NRN(right kink)	0.604	0.030	0.634
PRN(right kink)	0.582	0.030	0.612
NLP(left kink)	1.122	0.031	1.153
NLN(left kink)	0.601	0.031	0.632
PLN(left kink)	0.106	0.031	0.137

[a]The perpendicular model gives 0.030 eV.
[b]See Eq. (3).

formation energy by 0.006 eV when we increase the length of the simulation cell from $136b$ ($L_A=63b$, $L_B=10b$, and $L_C=63b$) to $150b$ ($L_A=70b$, $L_B=10b$, and $L_C=70b$). Thus our calculated kink formation energies are well converged with the length of the simulation cells in the [111] direction.

A kink pair in $1/2a\langle 111\rangle$ screw dislocations consists of a left kink and a right kink. If the separation between the left and right kink is sufficiently large, the formation energy of a kink pair is just the sum of the formation energies of the two component kinks. Since there are 4 kinds of left kinks and 4 kinds of right kinks, there are 16 ways to combine pairs of kinks. In some cases, one or two flips are required to fulfill the requirement of the dislocation core configuration when the kink pair nucleates from a perfect dislocation. Figure 8 schematically lists 16 kinds of kink pairs and their formation energies.

C. Relation of kinks

1. Structural analysis

Figure 9 displays the strain energy profile for dislocation quadruples containing various right kinks along the dislocation lines. The strain energy is computed by summing the atomic strain energies for all atoms in each $1b$ thick slice region along the dislocation line. For comparison, the strain energy distribution of a perfect dislocation quadruple in the same size simulation cell is also plotted. These figures show the following.

(1) The *NRP* kink [Fig. 9(a)] has a single strain energy maximum at its formation region.

(2) The *NRN* kink [Fig. 9(b)] has a strain energy maximum at the formation region and a strain energy minimum above its formation region.

(3) The *PRN* kink [Fig. 9(c)] has a strain energy maximum at the kink formation region and strain energy minima

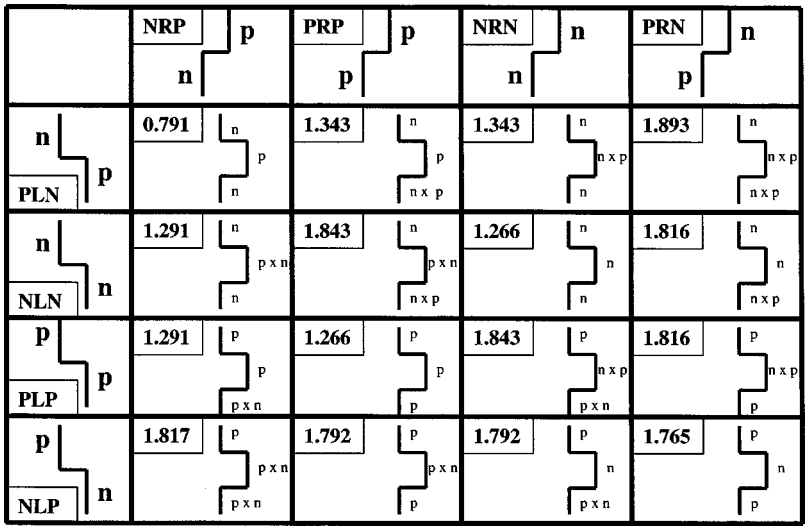

FIG. 8. Calculated formation energies of all kink pairs in the asymmetric core screw dislocations in Ta. The kink pair formation energy is the summation of the formation energies of the component single kinks and the required flips. Note that the kink pair *PLN-NRP* has the lowest formation energy, which is 0.475 eV lower than the second lowest kink pair formation energy.

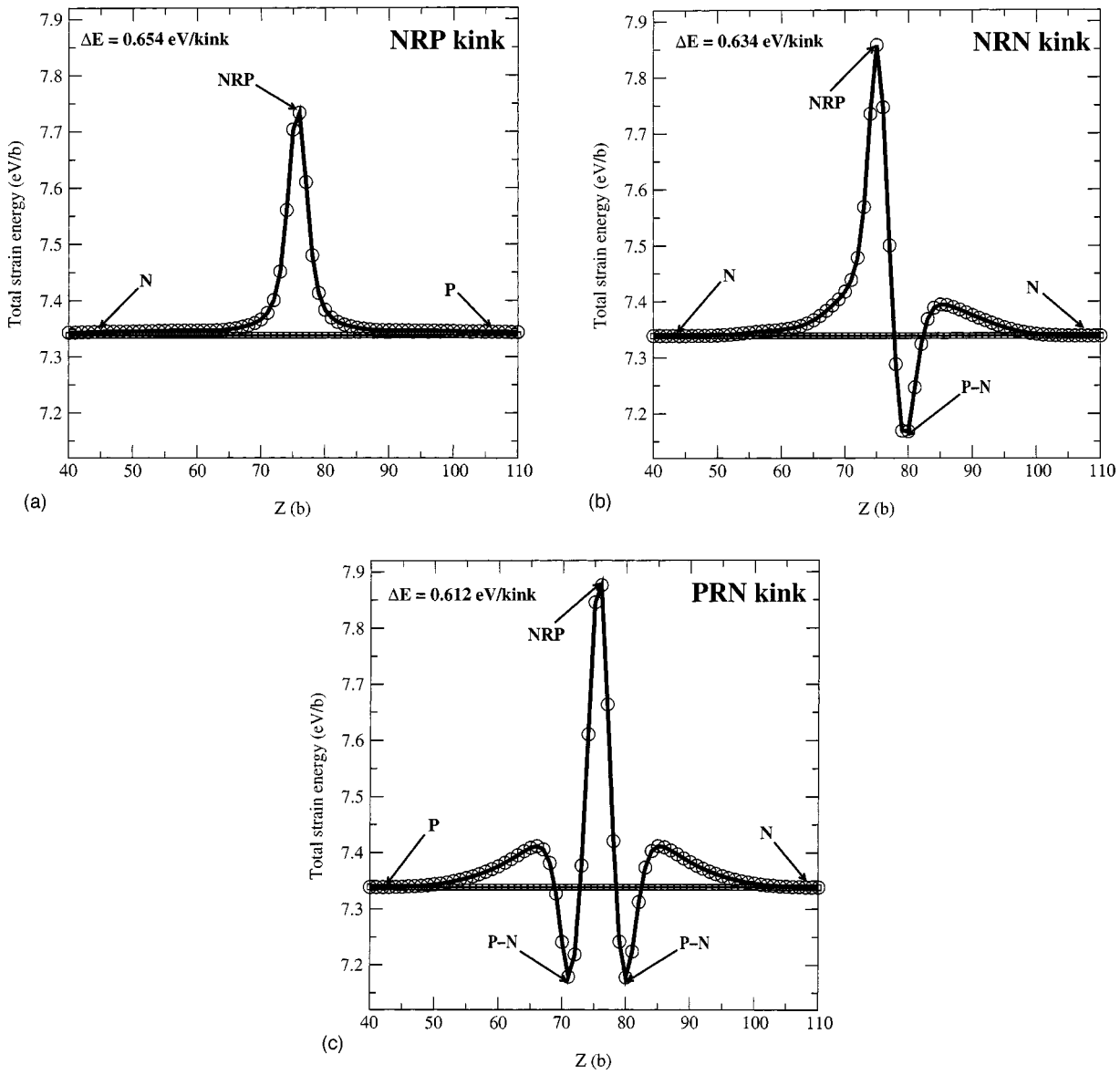

FIG. 9. The strain energy distribution for dislocation quadruples with right kinks. (a) The *NRP* kink, (b) the *NRN* kink, and (c) the *PRN* kink.

on both sides of the formation region.

A similar analysis in Fig. 10 shows the strain energy distributions along the dislocation quadruples with various left kinks. These figures show a strain energy minimum at the *PLN* kink formation region and a superficial resemblance of the strain energy distributions for the *NLN* and *NLP* kinks (i.e., there is only a strain energy maximum at the kink formation region).

Figure 11 shows the DD maps with various features of the core configurations in the screw dislocation with kinks and flips. Figure 11(a) displays the dislocation core configuration in the central region of the kinks ($Z=75b$ of the simulation cells). Although the directions of the kink vectors (pointing from the equilibrium dislocation center in region *A* to the equilibrium dislocation center in region *C* as indicated in Fig. 1) for the left and right kinks are different, the left and right kinks could have the similar dislocation core configurations at the center of the kinks (where the center of the screw dislocation lies just in between two neighboring equilibrium positions). In fact, we find that all types of kinks have identical DD maps at this position. Figures 11(b) and 11(c) show DD maps in the regions surrounding the kink center (indicated as *P-N* in Fig. 9 and *N-P* in Fig. 10). We find that the dislocation core configurations in Figs. 11(b) and 11(c) resemble that in the center of the flips [Fig. 11(d)] and are similar to the nonpolarized symmetric core. Hence, we find that the strain energy minima for the right kinks in Fig. 9 actually correspond to a low energy *P-N* flip. We also find the *N-P* flip in some left kinks (*NLN*, *PLP*, and *NLP*).

On the basis of the above analysis some kinks are composed of a kink and flips. The relation of the right and left kinks in $1/2a\langle 111\rangle$ screw dislocations can be summarized as in the following equations:

$$NRN = NRP + P\text{-}N, \tag{6a}$$

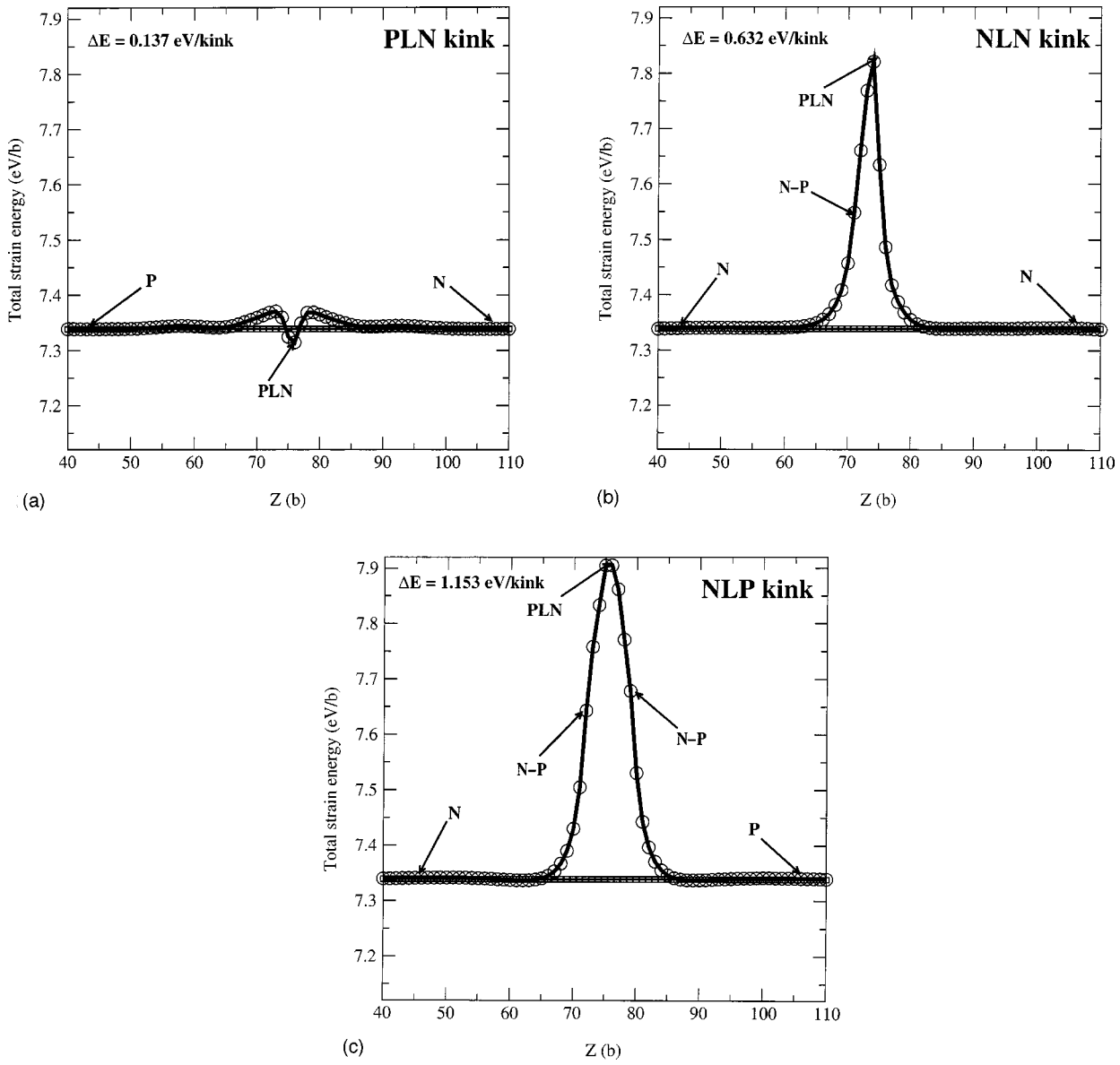

FIG. 10. The strain energy distribution for the dislocation quadruples with left kinks. (a) the *PLN* kink, (b) the *NLN* kink, and (c) the *NLP* kink.

$$PRP = P\text{-}N + NRP, \tag{6b}$$

$$PRN = P\text{-}N + NRP + P\text{-}N, \tag{6c}$$

$$NLN = N\text{-}P + PLN, \tag{6d}$$

$$PLP = PLN + N\text{-}P, \tag{6e}$$

$$NLP = N\text{-}P + PLN + N\text{-}P. \tag{6f}$$

These equations indicate that the *NRP* kink is the elementary right kink with all other right kinks being composites consisting of the *NRP* kink plus one or two *P-N* flips; the *PLN* kink is the basic left kink with all other left kinks being combinations of the *PLN* kink plus one or two *N-P* flips.

2. Comparison to other calculations

The kink relationship for asymmetric core dislocations in Eq. (6) provides the first such connection from atomistic level simulations. Although these relations were obtained using the *q*EAM1 FF for Ta, they provide a universal pattern for all bcc metals. To prove this point, we compared all available kink formation energy data in bcc metals from the literature.

A direct corollary of Eq. (6) is that the kink formation energy differences $\Delta E^{NRN} - \Delta E^{NRP}$, $\Delta E^{PRN} - \Delta E^{NRN}$, and $(\Delta E^{PRN} - \Delta E^{NRP})/2$ should be nearly equal and close to the *P-N* flip formation energy $\Delta E^{P\text{-}N}$ and the kink formation energy differences $\Delta E^{NLN} - \Delta E^{PLN}$, $\Delta E^{NLP} - \Delta E^{NLN}$, and $(\Delta E^{NLP} - \Delta E^{PLN})/2$ should be similarly close to the formation energy of the *N-P* flip ($\Delta E^{N\text{-}P}$). It should be mentioned that the flip in the composite kinks (*NRN*, *PRP*, *PRN*, *NLN*,

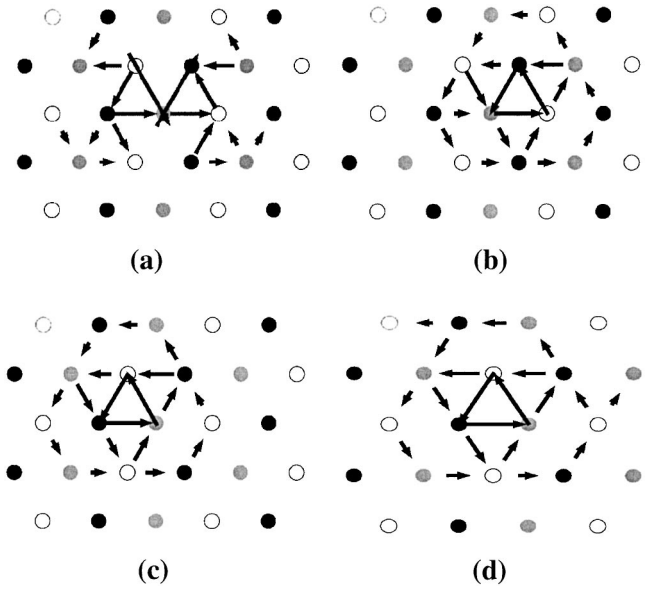

FIG. 11. The differential displacement maps of the dislocation core at the regions with characteristic features along the asymmetric core $1/2a[111]$ screw dislocation. The figure (a) shows the atomic relative displacements at the center of the kink formation region ($Z=75b$) while (b) and (c) indicate the flips in the kink formation region (indicated as *P-N* in Figs. 9 and *N-P* in Figs. 10) at different dislocations. (d) The DD map for the isolated flips along the asymmetric core screw dislocations.

PLN, and *NLP*) is under the different environments from the isolated flip. The kinks and the flips are only separated by $3b$ in the composite kinks. The close interaction between the flip and the kink might relax the total strain energy, such that the kink formation energy differences could be smaller than the corresponding isolated flip formation energy (see Table III).

Table IV compares the formation energies of the isolated flips and the flips in the composite kinks. Both our results (for Ta) and those by Rao *et al.*[19] (for Mo) show the expected relation of the flip formation energies. We used the qEAM1 FF for Ta as well as the periodic/fixed boundary conditions in this work, while Ref. 19 employed the MGPT FF for the Mo and Green's function boundary conditions. The agreement between these two simulations indicates that the relation of Eq. (6) is independent of the employed force fields and boundary conditions.

However, the results by Yang *et al.*[9] using the MGPT FF for Ta do not show the expected behavior of the flip formation energies. Neither do the older calculations by Duesbery[17] for K and α-Fe. There are two possible reasons for this discrepancy. First, the equilibrium dislocation core in our study and Ref. 19 has a large polarization while the dislocation polarization is very small ($\sim$0.0042) in Ref. 9. A smaller polarization of the dislocation implies a smaller difference among the kinks in the same category (left or right). The composite kinks might not dissociate into a flip and an elementary kink when the dislocation core is only weakly polarized. The second reason could be the incomplete relaxation of the atomistic structures. Duesbery in Ref. 17 used fixed boundaries where atoms are fixed at the positions determined by anisotropic elasticity theory in the simulation. These fixed boundaries could introduce bias in the atomistic relaxation if the simulation cells were not sufficiently large in three dimensions.

Reference 35 found the following order of kink pair formation energies:

$$PLN\text{-}NRP < NLN\text{-}NRN < NLP\text{-}PRN. \tag{7}$$

However, no atomistic explanation was proposed. It is straightforward to interpret the above equation using the kinks relations. The kink pair *NLN-NRN* can be considered as the combination of the kink pair *PLN-NRP* with a pair of *N-P* and *P-N* flips. Similarly, the kink pair *NLP-PRN* can be considered as the kink pair *NLN-NRN* plus a pair of the *N-P* and *P-N* flips. Therefore, assuming that a pair of *N-P* and *P-N* flips contributes positive strain energy to the composite

TABLE IV. Comparison of the formation energies (in eV) of the flips under different environments.

Materials	K[a] (Duesbery)	α-Fe[a] (Duesbery)	Mo[b] (Rao *et al.*)	Ta[c] (Yang *et al.*)	Ta (present work)
			P-N flip		
$\Delta E^{P\text{-}N}$	0.048	0.300	0.00	0.03	0.005
$\Delta E^{NRN}-\Delta E^{NRP}$	0.043	0.267	−0.16	−0.11	−0.020
$\Delta E^{PRN}-\Delta E^{NRN}$	−0.022	−0.085	−0.15	0.20	−0.022
$\frac{1}{2}(\Delta E^{PRN}-\Delta E^{NRP})$	0.011	0.091	−0.16	0.05	−0.021
			N-P flip		
$\Delta E^{N\text{-}P}$	0.018	0.408	0.21	0.23	0.572
$\Delta E^{NLN}-\Delta E^{PLN}$	0.028	−0.322	0.18	0.19	0.495
$\Delta E^{NLP}-\Delta E^{NLN}$	0.045	0.126	0.21	0.08	0.521
$\frac{1}{2}(\Delta E^{NLP}-\Delta E^{PLN})$	0.037	−0.098	0.20	0.14	0.508

[a]Reference 17, using a first-principle interatomic potential for potassium and an empirical interatomic potential for iron.
[b]Reference 19, using the MGPT FF.
[c]Reference 9, using the MGPT FF.

TABLE V. Comparison of formation energies of kink pairs. In the table, "yes/no" indicates whether the calculated kink pair formation energies do or do not obey the rule $\Delta E^{PLN\text{-}NRP} < \Delta E^{NLN\text{-}NRN} < \Delta E^{NLP\text{-}PRN}$.

Materials	$\Delta E^{PLN\text{-}NRP}$ (eV)	$\Delta E^{NLN\text{-}NRN}$ (eV)	$\Delta E^{NLP\text{-}PRN}$ (eV)	yes/no
K[a] (Duesbery)	0.076	0.147	0.170	Yes
α-Fe[a] (Duesbery)	0.241	0.186	0.227	No
Mo[b] (Rao *et al.*)	1.62	1.64	1.70	Yes
Ta[c] (Yang *et al.*)	0.96	1.04	1.32	Yes
Ta (present work)	0.791	1.266	1.765	Yes
α-Fe[d] (Wen *et al.*)	0.84	1.29	1.94	Yes

[a]Reference 17, using a first-principle interatomic potential for potassium and an empirical interatomic potential for iron.
[b]Reference 19, using the MGPT FF.
[c]Reference 9, using the MGPT FF.
[d]Reference 35, using a nudged elastic band method and an EAM potential.

kinks leading to the increasing order in Eq. (7). Indeed, Eq. (7) is universal as demonstrated by Table V. All available kink pair formation energies, except for α-Fe in Ref. 17, follow the same trend. Since this sole exception (the empirical potential for iron) yields negative formation energy for two kinds of kinks, we consider this potential to be flawed. On the other hand, the kink pair formation energies in K, Mo, Ta, and α-Fe all obey the rule (7).

V. KINKS IN SYMMETRIC CORE SCREW DISLOCATIONS

The symmetric core has zero polarization and is nondegenerate. As a result there are only two types of kinks (left kink and right kink) and no (polarization) flip in $1/2a\langle 111\rangle$ symmetric core screw dislocations. We obtained relaxed kink configurations for the symmetric core screw dislocations using the qEAM2 and qEAM3 FFs and the same periodic/fixed boundary simulation technique.

Table VI gives our results of the height, width, and formation energies for various kinks in the symmetric core screw dislocations. To evaluate the kink geometrical parameters, we derived the line shape of the kinks by calculating the atomic-strain energy-weighted center of the twelve atoms with the highest strain energies for each $1b$ slice along the dislocation line. This way to define the dislocation position might seem inconsistent with the observation in Sec. III A 4 that a symmetric dislocation core has only six atoms with highest atomic strain energies in a straight screw dislocation. However, we must also describe the dislocation core configurations in the kink region, such as the state shown in Fig. 11(a). For the latter case, using the twelve (rather than six) highest energy atoms allows a better description. Indeed, using the twelve-atom definition does not lead to any problem in calculating the equilibrium symmetric core dislocation position since the central six atoms have atomic strain energies four times larger than others. The calculated heights of the symmetric core kinks are exactly equal to $|1/3a\langle 112\rangle|$ (2.74 Å for the qEAM2 FF and 2.71 Å for the qEAM3 FF).

TABLE VI. Comparison of the kink height h, the kink width w, the isolated kink formation energies, and the kink pair formation energies from the various qEAM FFs calculations. The *PLN* is considered as the left kink and the *NRP* as right kink in the qEAM1 FF simulations. The kink formation energies have been corrected for kink-kink interactions using Eq. (4).

Force fileds	qEAM1	qEAM2	qEAM3
	Left kink		
height h (Å)	2.71	2.74	2.71
width w (b)	9.1	11.4	11.3
formation energy ΔE (eV)	0.137	0.304	0.373
	Right kink		
height h (Å)	2.71	2.74	2.71
width w (b)	10.4	13.6	14.0
formation energy ΔE (eV)	0.654	0.124	0.269
	Kink pair		
formation energy ΔE (eV)	0.791	0.428	0.642

Comparing the results in Table VI for the asymmetric core kinks and the symmetric core kinks, we find that the symmetric core kinks span a larger distance ($11.4b$ for the left kink and $13.8b$ for the right kink in average) along the dislocation line than the asymmetric core kinks ($9.1b$ for the left kink and $10.4b$ for the right kink). Most importantly, the kink pair formation energies for the symmetric core dislocations (0.428 eV from the qEAM2 FF and 0.642 eV from the qEAM3 FF) are smaller than 0.791 eV from the qEAM1 FF for the asymmetric core dislocations. This is reasonable because that the polarization of the asymmetric dislocation core causes some atoms to be in compression or tension in the kink formation region (this has been pointed out and discussed in Ref. 16) and would lead to higher kink pair formation energy for the asymmetric core dislocation than the symmetric core dislocation. Although the qEAM2 and qEAM3 FF predict similar equilibrium symmetric core structures, they lead to different kink pair formation energies. This implies besides the equilibrium dislocation core structure some other factors also underlie the kink pair formation process. In this work, we observed that increasing the core polarization curvature from the qEAM2 FF to the qEAM3 FF leads to increase the kink pair formation energy by 0.214 eV. This correlates with the fact the Peierls stress for straight dislocations also increases with increasing core polarization curvature (see Ref. 25).

VI. CONCLUSIONS AND DISCUSSIONS

This paper reports our calculations on the multiplicity, structural features, and formation energies of $1/3a\langle 112\rangle$ kinks in $1/2a\langle 111\rangle$ screw dislocations with different core structures (asymmetric core and symmetric core).

Two degenerate asymmetric cores for $1/2a\langle 111\rangle$ screw dislocations lead to 2 types of (polarization) flips, 8 kinds of isolated kinks and 16 combinations of kink pairs. Among the eight isolated kinks, we find that the *NRP* kink is the elementary right kink, the *PLN* kink is the basic left kink, and the

others are the composites of the elementary kinks and flips.

In contrast, for screw dislocations with symmetric core there is only one right kink, one left kink, and one kind of kink pair. We find the kink pair formation energies for the symmetric core dislocations (0.428 eV from the *q*EAM2 FF and 0.642 eV from the *q*EAM3 FF) are smaller than 0.791 eV from the *q*EAM1 FF for the asymmetric core dislocations, indicating the equilibrium dislocation core structure is an important factor in determining the kink pair formation energy in bcc Ta. Furthermore, we find that the calculated kink pair formation energies for the two symmetric cores studied differ by as much as 0.214 eV (based on the two force fields leading to similar equilibrium symmetric cores but different core polarization curvature) implying that core polarization curvature may also be a critical quantity in determining kink formation energies.

All our calculated kink pair formation energies are lower than the experimental result [0.98 eV (Ref. 36)]. However, the determined kink height in that measurement was 1.74 times the value $|a/3\langle 112\rangle|$ for the unit kink height in our study. Thus the experimental formation energy for a pair of kinks connecting the nearest neighboring positions might be lower than 0.98 eV and might agree with our result. In the mesoscopic simulation by Tang *et al.*[37] the zero temperature kink pair activation enthalpy was determined to be 1.08 eV, much higher than our results. Stainier *et al.*[38] found that the kink pair formation energy of 0.70 eV (only 9% higher than our result from the *q*EAM3 FF) by optimally fitting to the experimental data of Mitchell and Spitzig[39] (temperature dependence of stress-stain curves and strain-rate dependence of stress-strain curves) in their micromechanical model.

All three *q*EAM FFs for Ta in this work reproduce the *ab initio* results of (i) zero temperature energy and pressure as a function of volume (including large compressions and expansions) for various phases bcc, fcc, and *A*15, (ii) elastic constants, (iii) vacancy and surface formation energies, (iv) energetics of a shear deformation in the twinning direction that takes the bcc crystal back to itself, and (v) the $\langle 111\rangle/\{112\}$ and $\langle 111\rangle/\{110\}\gamma$ surfaces. However, only *q*EAM2 and *q*EAM3 FFs lead to the symmetric core structures for $1/2a\langle 111\rangle$ screw dislocations, similar to the *ab initio* results. Furthermore, the curves of core energy variations with polarization in Fig. 6 show that the results using the *q*EAM3 FF agree best with the *ab initio* results among the three *q*EAM FFs in this work. Therefore, the *q*EAM3 FF is the best first-principle potential for Ta in this work and suitable to study the properties of screw dislocations.

Table II shows that the *q*EAM3 FF leads to the Peierls stresses in best agreement with the *ab initio* results comparing to all other potentials (MGPT, *q*EAM1, and *q*EAM2). Hence, we expect the kink pair formation energy (0.642 eV) from our *q*EAM3 FF to be accurate and in close agreement with *ab initio* calculations. Since the equilibrium dislocation core structure and the core polarization curvature both are important in accurately determining kink-pair formation energy, we propose that the *ab initio* data of the energy variation with dislocation core polarization (shown in Fig. 6 for Ta) should be included in the future potential development for bcc metals.

ACKNOWLEDGMENTS

This research was funded by a grant from DOE-ASCI-ASAP. The facilities of the MSC were also supported by grants from NSF (Grant Nos. CHE 9985574 and CHE 9977872), ARO (MURI), ARO (DURIP), Chevron-Texaco Corp., General Motors, Beckman Institute, and Asahi Kasei.

*Current address: Materials Sciences Division, Lawrence Berkeley National Laboratory, Berkeley, CA 94720

†Current address: Los Alamos National Laboratory, Los Alamos, NM 87545.

‡ Author to whom correspondence should be addressed. Email address: wag@wag.caltech.edu

[1] V. V. Bulatov and L. P. Kubin, Curr. Opin. Solid State Mater. Sci. **3**, 558 (1998).

[2] R. Phillips, D. Rodney, V. Shenoy, E. Tadmor, and M. Ortiz, Modell. Simul. Mater. Sci. Eng. **7**, 769 (1999).

[3] M. I. Baskes, Curr. Opin. Solid State Mater. Sci. **4**, 273 (1999).

[4] A. M. Cuitino, L. Stanier, G. Wang, A. Strachan, T. Çağin, W. A. Goddard, and M. Ortiz, J. Comput.-Aided Mater. Des. **8**, 127 (2002).

[5] V. V. Bulatov, S. Yip, and A. S. Argon, Philos. Mag. A **72**, 453 (1995).

[6] J. A. Moriarty, W. Xu, P. Söderlind, J. Belak, L. H. Yang, and J. Zhu, J. Eng. Mater. Technol. **121**, 120 (1999).

[7] F. Louchet and L. P. Kubin, Philos. Mag. A **39**, 433 (1979).

[8] W. Xu and J. A. Moriarty, Comput. Mater. Sci. **9**, 348 (1998).

[9] L. H. Yang, P. Söderlind, and J. A. Moriarty, Philos. Mag. A **81**, 1355 (2001).

[10] K. Ito and V. Vitek, Philos. Mag. A **81**, 1387 (2001).

[11] G. Wang, A. Strachan, T. Çağın, and W. A. Goddard, Mater. Sci. Eng., A **309**, 133 (2001).

[12] T. Suzuki, Y. Kamimura, and H. O. K. Kirchner, Philos. Mag. A **79**, 1629 (1999).

[13] A. Seeger and P. Schiller, *Physical Acoustics*, edited by W. P. Mason (Academics, New York, 1966), Vol. 3A, p. 361.

[14] H. R. Kolar, J. C. H. Spence, and H. Alexander, Phys. Rev. Lett. **77**, 4031 (1996).

[15] A. Seeger and C. Wuthrich, Nuovo Cimento Soc. Ital. Fis., B **33**, 38 (1976).

[16] M. S. Duesbery, Acta Metall. **31**, 1747 (1983).

[17] M. S. Duesbery, Acta Metall. **31**, 1759 (1983).

[18] M. S. Duesbery and Z. S. Basinski, Acta Metall. Mater. **41**, 643 (1993).

[19] S. I. Rao and C. Woodward, Philos. Mag. A **81**, 1317 (2001).

[20] V. Vitek, Cryst. Lattice Defects **5**, 1 (1974).

[21] W. Xu and J. A. Moriarty, Phys. Rev. B **54**, 6941 (1996).

[22] M. S. Duesbery and V. Vitek, Acta Mater. **46**, 1481 (1998).

[23] S. Ismail-Beigi and T. A. Arias, Phys. Rev. Lett. **84**, 1499 (2000).

[24] C. Woodward and S. I. Rao, Philos. Mag. A **81**, 1305 (2001).

[25] G. Wang, A. Strachan, T. Çağın, and W. A. Goddard, Phys. Rev. B **67**, 140101(R) (2003).

[26] J. P. Hirth and J. Lothe, *Theory of Dislocations* (Krieger, Melbourne, FL, 1982), p. 162.

[27] W. Sigle, Philos. Mag. A **79**, 1009 (1999).

[28] S. Chantasiriwan and F. Milstein, Phys. Rev. B **53**, 14 080 (1996).

[29] A. Strachan, T. Çağın, O. Gülseren, S. Mukherjee, R. E. Cohen, and W. A. Goddard (unpublished).
[30] J. Perdew and A. Zunger, Phys. Rev. B **23**, 5048 (1981).
[31] M. Ceperley and B. J. Alder, Phys. Rev. Lett. **45**, 566 (1980).
[32] D. R. Hamann, Phys. Rev. B **40**, 2980 (1989).
[33] S. G. Louie, S. Froyen, and M. L. Cohen, Phys. Rev. B **26**, 1738 (1982).
[34] G. Wang, Ph.D. Thesis, Caltech, 2002.
[35] W. Wen and A. H. W. Ngan, Acta Mater. **48**, 4255 (2000).
[36] M. Werner, Phys. Status Solidi A **104**, 63 (1987).
[37] M. Tang, L. P. Kubin, and G. R. Canova, Acta Mater. **46**, 3221 (1998).
[38] L. Stainier, A. M. Cuitino, and M. Ortiz, J. Mech. Phys. Solids **50**, 1511 (2002).
[39] T. E. Mitchell and W. A. Spitzig, Acta Metall. **13**, 1169 (1965).
[40] *Single Crystal Elastic Constants and Calculated Aggregate Properties: A Handbook*, edited by G. Simmons and H. Wang (MIT Press, Cambridge, MA, 1971).
[41] C. Woodward and S. I. Rao, Phys. Rev. Lett. **88**, 216402 (2002).